Article

Applied Spectroscopy

Applied Spectroscopy
2020, Vol. 74(12) 1515–1529

DOI: 10.1177/0003702820945018
journals.sagepub.com/home/asp
SAGE

Qualitative and Semiquantitative Determination of the Atomic and Molecular Tungsten Distributions in Hybrid Hydroxyurethanes–Poly(dimethylsiloxane) Films Containing Phosphotungstates ($[PW_{12}O_{40}]^{3-}$)

Orlando Elguera Ysnaga[1], Kelen M.F. Rossi de Aguiar[2], Cibele Bugno Zamboni[3], Wagner Luiz Polito[1], and Ubirajara P. Rodrigues-Filho[1]

Abstract

In this study, hybrid poly(dimethylsiloxane)-derived hydroxyurethanes films (PDMSUr-PWA) containing phosphotungstic acid ($H_3PW_{12}O_{40}$/PWA) were characterized using field emission gun scanning electron microscopy (FEG-SEM), in attenuated total reflectance Fourier transform mid-infrared mode (ATR FT-MIR), and analyzed using synchrotron radiation micro-X-ray fluorescence (SR-μXRF), synchrotron radiation grazing incidence X-ray fluorescence (SR-GIXRF), laser-induced breakdown spectroscopy (LIBS), and instrumental neutron activation analysis (NAA) in order to correlate the distribution patterns of tungsten and properties of PDMSUr-PWA films. PDMS constitute elastomers with good mechanical, thermal, and chemical (hydrophobicity/non-hygroscopy) resistance. Currently, products based on urethanes (e.g., polyurethanes) are widely used in many applications as plastics, fiber-reinforced polymers, high-performance adhesives, corrosion-resistant coatings, photochromic films, among others. The possibility to combine inorganic and organic components can produce a hybrid material with unique properties. PWA has an important role as agent against the corrosion of steel surfaces in different media, besides exhibiting amazing catalytic and photochromic properties in these films. PWA kept its structure inside of these hybrid films through interactions between the organic matrix of PDMSUr and silanol from the inorganic part (organically modified silica), as was shown using ATR FT-MIR spectra. The FEG-SEM/SR-μXRF/wide-angle X-ray scattering (WAXS)/X-ray diffraction (XRD)/energy dispersive X-ray results proved the presence of PWA in the composition of domains of PDMSUr-PWA films. At PWA concentrations higher than 50 wt%/wt, tungsten segregation across the thickness is predominant, while that at PWA concentrations lower than 35 wt%/wt, tungsten segregation at surface is predominant. Inhomogeneities in the tungsten distribution patterns (at micrometric and millimetric level) may play an important role in the mechanical properties of these films (elastic modulus and hardness).

Keywords

Hydroxyurethanes–poly(dimethylsiloxane) films, PDMSUr-PWA films, synchrotron radiation micro-X-ray fluorescence, SR-μXRF, instrumental neutron activation analysis, NAA, laser-induced breakdown spectroscopy, LIBS, hybrid materials

Date received: 3 March 2020; accepted: 19 June 2020

Introduction

Polyurethanes (PUs) constitute a group of phase segmented polymers that exhibit very interesting mechanical and chemical properties.[1] Products made of PU are widely used all over the world as high-performance adhesives, coatings, and elastomers. PU is a kind of high polymer with a basic repetitive unit urethane bond, represented

[1]Institute of Chemistry of São Carlos, University of São Paulo (IQSC-USP), São Carlos, Brazil
[2]Federal University of Technology–Paraná (UTFPR), Toledo, Brazil
[3]Nuclear and Energetic Research Institute (IPEN/CNEN-SP), São Paulo, Brazil

Corresponding author:
Orlando Elguera Ysnaga, Universidade de São Paulo, Av. Trabalhador São-Carlense 400, CEP 13566-590, Sao Paulo, São Carlos 05508-900, Brazil.
Email: orlandoelguera@gmail.com

by –NHCOO–. Traditionally, PUs are produced from the polymerization of isocyanates, polyols, and some additives. PUs exhibit a two-phase microstructure, which arises from the chemical incompatibility between the soft and the hard segments.[1] Rigid segments segregate into a glassy or semi-crystalline domain dispersed in amorphous or rubbery matrices formed by soft segments.[2] Because PUs are highly flammable and the flame spread quite fast in case of fire, potentially hazardous vapor and smoke may be emitted from the breakdown of PU materials. Urethane bond groups of rigid PUs start to break up into small components from isocyanates and polyols, about of 150 °C to 180 °C.[3] In this context, a rising demand for materials which do not present such inconvenience or present higher resistance to thermal degradation has been observed. New materials or the modification of the already stated routes be explored.[4] In addition, a great deal of effort has been done to obtain by greener routes. Among the possible routes, the less aggressive route ruling out the use of toxic isocyanate which is based on ring opening polymerization has been applied.[5,6] The advantage of such route is to recycle a residual gas, carbon dioxide (CO_2), converting it into cyclic carbonates for further reaction with amines, giving rise to the isocyanate free hydroxypolyurethanes.[7] The chemical fixation and transformation of CO_2 is an attractive approach from environment and economic viewpoints. CO_2 is a cheap, non-toxic, and available carbon source.[8] Polysiloxanes are known to reduce the liberation of heat by forming films with low thermal diffusivity and permeability to the oxidizing agents in a mechanism called char formation. Polydimethylsiloxane (PDMS) is one of the most known polysiloxanes, with properties based on the features of siloxane bond. Such properties can be listed as low glass transition temperature (T_g), low surface energy, hydrophobicity, high gas permeability, insulating properties, oxidative and thermal stability, and biocompatibility. PDMS can be considered inert, non-toxic, and non-flammable. Mechanical properties of oligomers and polymers containing PDMS present some limitations, such as low hardness and tenacity, unless they are reinforced with silica or vulcanized.[9–11] A way to introduce PDMS segments and silicate nanofillers is initially to prepare cyclic carbonates from an epoxydic reagent bearing PDMS, as published by our group.[12] Aminosilanes, such as 3-aminopropyltriethoxysilane, are nucleophiles and can play a role opening the cyclic carbonate ring to form urethane bonds. In addition, during the sol–gel process, organically modified silica (ormosil) domains are produced by hydrolysis and condensation of the alkoxy groups. The chemical nature of the aminosilane can confer to the final product valuable physical–chemical properties such as thermal resistance, hardness, corrosion protection, among others.[13] The insertion of PDMS and alcoxysilyl terminal groups in a unique oligomeric backbone makes possible to obtain a hybrid inorganic–organic silicone polyurethane (PDMSUr). Ormosil or silicate regions act as a reinforcement agent for the hybrid material as much as by crosslinking as by introducing a harder ceramic component based on the silicate structure,[4] besides to increase thermal stability of the PU.[14] This hybrid PU can host polyoxometalates, such as phosphotungstic acid ($H_3PW_{12}O_{40}$), which are an interesting class of photochromic materials and they also present catalytic properties. Hydrated $H_3PW_{12}O_{40}$ is highly soluble in water, being well stabilized in inorganic crosslinks, such silicate network, through Coulombic interactions.[15] According to Rossi de Aguiar et al.,[13] the incorporation of phosphotungstic acid (PWA) produced a hard material (20–60 MPa) and its elastic modulus rose by more than a hundred times as the PWA content increased. PWA has also an important role in the properties of coatings, based on PDMSUr-PWA films, against corrosion of steel surfaces in different media.[13] Phosphotungstate composites also have been exploited in our group as new antifungal and antibacterial coatings with broad anti-microorganism activity, thus reinforcing the importance for development of fast and reliable methodologies for characterization of such composites.[16]

X-rays are high-energy electromagnetic waves whose magnitude of wavelengths are in the order of tenths of nanometers (nm), allowing for the analysis of atoms and chemical bonds. According to their energy, X-rays are classified as hard X-rays (10–120 keV/wavelength 0.10–0.01 nm, respectively) and soft X-rays (energy $<$ 10 keV/wavelength $>$ 0.10 nm). The interactions between X-rays and matter provide information about the composition of the sample and the position of the atoms in it.[17] X-ray fluorescence (XRF) is a powerful method for determination of the chemical composition of objects that are either too thick for transmission–absorption measurements or are insulating and therefore preclude photoemission techniques. XRF analysis also enables scanning methods based on the use of tightly focused incident beams. In X-ray microspectroscopy, the spectral response of a defined position is probed by the X-ray microbeam.[18] Micro-X-ray fluorescence (μXRF) makes possible the mapping of microregions, and therefore, the analysis of heterogeneous materials.[19] Patterson et al. used μXRF and FT-IR cross-sectional imaging in order to characterize the distribution of a stannate (stannous 2-ethylhexanoate) catalyst in PDMS foams, which constituted the base to establish the mechanism of migration of this catalyst.[20] Patterson et al. obtained three-dimensional (3D) mapping of silicon (Si) in PDMS foams using confocal μXRF. These authors mapped the densities (correlating them with the scattering intensities) of low atomic number (Z) elements in materials such as PDMS foams and aerogels.[21] μXRF laboratory spectrometers possesses lateral resolutions at the range (10–100 μm). However, these resolutions are lesser than those obtained by synchrotron radiation micro-X-ray fluorescence (SR-μXRF).

Synchrotron radiation (generated in storage rings from high energetic electrons) is a very intense source of X-rays.[22] Synchrotron has a much higher brilliance (number of photons emitted/energy interval/second)/(unit of solid angle 5 (unit of size source) than produced by laboratory-based sources (X-ray tubes); therefore, they are more suitable for producing microbeams. Indeed, in the last four decades, there has been an increase in the brilliance of synchrotron radiation to conventional sources by a factor of 10^{14}, resulting in intensities 10^4–10^5 times greater than the intensities produced in laboratory spectrometers. For SR-μXRF, an important property is the high degree of polarization of synchrotron radiation, which improves the signal-to-noise ratio significantly and the sensitivity is improved by orders of magnitude.[19,22] Synchrotron radiation-assisted spectroscopy include regions range from infrared to X-rays, covering energies from some eV to dozens of KeV, respectively. This spectroscopy constitutes one of the most powerful tools in experiments involving imaging or microscopy in physics, biology, medicine, nanotechnology, catalysis, among others.[23] In X-ray fluorescence spectromicroscopy, such as μXRF assisted by synchrotron (SR-μXRF), the dispersed XRF signal is mapped out spatially. In SR-μXRF spectrometers, the white (polychromatic) or monochromatic beam of the synchrotron can be collimated until reaching dimensions in the range of a few micrometers.[24] SR-μXRF integrated signal depends on the excited atoms distributed throughout the volume of the material.[25] If a conventional X-ray source (such as the X-ray tube) is used for this purpose, the collimation would result in an X-ray flow too low to be useful in XRF experiments.[26] Our research group earlier published the SR-μXRF mapping of phosphotungstates ($[PW_{12}O_{40}]^{3-}$) in the characterization of hybrid nanomaterials.[27,28]

In grazing angle X-ray fluorescence (GIXRF), the X-ray incident beam is almost parallel to surface of the sample at angles equal or slightly larger (two to three times) than the value of the critical angle of sample's support. GIXRF method is applied in the analysis of thin films, in order to obtain composition, density, and thickness.[29,30] Synchrotron radiation grazing incidence X-ray fluorescence (SR-GIXRF) has a higher sensitivity than laboratory GIXRF, due to its reducing spectral background noise and polarized radiation.[31] SR-GIXRF, unlike SR-μXRF, a bulk analysis method, depends on the quality of the surface of the material.[26] Kawai et al., using a combination of TXRF/XPS and assisted by an X-ray synchrotron beam, reported the angle dependence of photoelectron peak intensity for a system of bilayers tungsten–silicon (W/Si) on an Si wafer.[32] SR-GIXRF was already used in qualitative determination of hybrid nanomaterials in our research group.[33]

Laser-induced breakdown spectroscopy (LIBS) is based on the focusing of a pulsed laser beam of high intensity, generating plasma from the material.[34] LIBS constitutes a very fast analysis, applicable to gases, solids, and liquids, requires minimal or no sample preparation. Among the fields of LIBS are applications industrial processes, environmental analysis, biology forensic science, art conservation, etc. LIBS was used for chemical mapping as well as for mapping of nanoparticles.[34,35] LIBS and XRF have already been combined, in order to perform multielemental determinations in inorganic samples.[36]

Instrumental neutron activation analysis (NAA) is one of the most used methods in order to determine tungsten in different types of matrices through the decades.[37–41] NAA involves bulk analysis unlike SR-μXRF that constitutes a more sensitive method for surface analysis. In the case of XRF analysis, the maximum depth of analysis can reach from tens to hundredths of micrometers (depending on the average atomic number of the analyzed matrix). On the other hand, NAA is an analysis in which the beam of neutrons crosses whole depth of samples, thus, the depth of analysis is not a limiting factor. NAA is a useful analytical method to perform multielement analysis.

To better understand the chemical and mechanical properties of these materials, it is important to know their molecular and elemental distribution. In this sense, microspectroscopic and spectroscopic techniques may be useful.[42] In this study, a systematic analysis regarding the distribution of tungsten from $H_3PW_{12}O_{40}$ within the PU matrix were performed by means of field emission gun scanning electron microscopy (FEG-SEM), SR-μXRF, SR-GIXRF, LIBS, and instrumental NAA. These methods of analyses and characterizations were applied to gather all the information needed to comprehend the tungsten distribution and its effect on mechanical and chemical properties. Thus, the present study aims to add to the knowledge of phosphotungstate ($[PW_{12}O_{40}]^{3-}$) and tungsten (W) distributions in films of polydimethylsiloxane–urethanes (PDMSUr) containing phosphotungstates in order to correlate their distribution patterns with their properties.

Material and Methods

Materials

All reagents used to synthesize the precursor cyclic carbonate PDMS-derived, here labelled as CCPDMS, are described in Rossi Flores de Aguiar,[4] Aguiar et al.,[12] and Rossi Flores de Aguiar et al.[13] To obtain polyhydroxyurethanes PDMS-derived (PDMSUr), the following reactants were used: purified CCPDMS, 3-aminopropyltriethoxysilane (APTES, >98%, Sigma Aldrich), 3-aminomethyl-3,5,5-trimethylcyclohexylamine (IPDA, >99%, mixture of cis and trans, Sigma Aldrich), dimethylacetamide (DMAc, 99,5%, Vetec), nitrogen (N_2, >99%, White Martins), phosphotungstic acid hydrate (PWA, Sigma Aldrich) dried at 60 °C overnight.

Methods

The synthesis of the precursors CCPDMS followed the procedure described by Aguiar et al.[1,3,4,13] After purification of CCPDMS, 0.42 g (1 mmol) was mixed with 0.218 g (3 mmol) of APTES in a vial previously purged with N_2. The reaction mixture remained under stirring for 40 min at 70 °C. Different contents of PWA (detailed in Table I) were dissolved in 2 mL of DMAc, which were dispersed into the hybrid PU matrix and stirred for 24 h at 60 °C.

Characterizations

Attenuated Total Reflectance Middle Infrared Spectroscopy

Spectra were acquired using a Nicolet Nexus 470 spectrometer (range 650 cm^{-1}–4000 cm^{-1}, resolution 4 cm^{-1}, 64 scans; Thermo Fisher Scientific) equipped with a zinc selenide crystal, operating in attenuated total reflectance (ATR) mode.[4]

Field Emission Gun Scanning Electron Microscopy

Microstructural images of the samples were obtained using an Inspect F50 FEG-SEM, with an acceleration voltage of 15 kV, work distance of 10.2 ± 2 mm, an Everhardt Thornley secondary electron detector, and Apollo X energy dispersive X-ray fluorescence (EDXRF) detector. PDMSUr-PWA films were metalized with carbon in a Sputtering Q150E ES (60 s at 50 A).[4,13]

Table I. Characterization techniques/method of analysis for PDMSUr-PWA films.

Technique of characterization/ method of analysis	Technique/method
ATR FT-MIR	Characterization of the organic functional groups contained in the PDMSUr-PWA films and preservation of PWA structure.
FEG-SEM	Characterization of phosphotungstate (PWA) agglomerates within thickness of the PDMSUr-PWA films.
SR-μXRF	Mapping intensities and using the iterative method of fundamental parameters (FP) can be obtained at elemental concentrations (at depth of hundredths of μm).
SR-GIXRF	Allows the obtention of concentrations at surface level (at depth of tenths of nm).
LIBS	Semi-quantitative determination of tungsten in the PDMSUr-PWA films.
NAA	Allows the quantitative determination of tungsten in the PDMSUr-PWA films at bulk level.

Synchrotron Radiation X-ray Fluorescence and Synchrotron Radiation Micro-X-ray Fluorescence

Synchrotron radiation micro-X-ray fluorescence measurements were performed at the D09B (15°) bending-magnet XRF beamline of a Brazilian Synchrotron Light Source (LNLS, Campinas-Brazil) unit.[43] The experiments were done in air atmosphere at atmospheric pressure. The experimental setup for SR-μXRF analysis included:

(i) The intense radiation source (storage ring) of 1.4 GeV provides a polychromatic X-ray beam, in which photon flux ranging from 3.9×10^{10} to 2.31×10^{11} photons/s and an energy tuned at the range of 4–16 keV.
(ii) The microfocussing system consisted of a rotation/high-precision *x*,*y* translation stage of the sample driven by stepping motors in order to focalize; a sample chamber that can be evacuated in order to avoid the attenuation of X-rays and to suppress the scattered radiation by the air; two non-plane mirrors arranged at Kirkpatrick–Baez (KB) configuration; and a microscope in order to identify the sample region to be analyzed. In this setup, the elliptical microbeam had the dimensions 18 μm (major axis) × 9 μm (minor axis) approximately, with a working distance of about 0.1 m.[43]
(iii) The detection system consisted of a CANBERRA Si(Li) X-ray detector model SL30165, with a resolution of 165 eV at 5.9 keV, operating in transmission geometry and energy-dispersive mode. The detector additionally contains six sets of array foils (each array consists of eight foils of pure aluminum). The energy X-ray dispersive Si(Li) transmission detector was cooled by $N_{2(l)}$ to reduce the heat load.[43]
(iv) The two-dimensional SR-μXRF elemental maps were processed, collecting a number between 400 and 420 sampling points (each point represents one XRF spectrum) scanned at zig-zag mode. The acquisition time for each point was set to 5 s. The raw spectral data were analyzed using the Readcnfmca v.2.0 program, developed at the LNLS XRF Beamline, and PyMca X-ray fluorescence v.4.4 program, developed by the software group of the European Synchrotron Radiation Facility, in order to extract the μXRF intensities for each point measurement and process them into elemental maps, respectively.[43] The pixel size of the SR-μXRF maps was 26 μm.[42] For 3D representation of tungsten peaks, from the SR-μXRF maps, the corresponding integration was performed by PyMca software package.[44,45]

Synchrotron Radiation Grazing Incidence X-ray Fluorescence

The SR-GIXRF measurements were performed at the D09B (15°) bending-magnet XRF beamline of the Brazilian

Synchrotron Light Source (LNLS, Campinas-Brazil).[41] The experimental setup for SR-GIXRF analysis includes the 1.4 GeV source (storage ring); a monochromatic X-ray beam (beam size 0.1 mm V × 5.0 mm H), set at energy 11 keV for tungsten determination; and an HPGe detector, cooled by $N_{2(l)}$, operating in energy dispersion mode. The grazing angles range of SR-GIXRF measurements was 0.05°–0.2°.[44,45]

Energy Dispersive X-ray Fluorescence Spectrometry (EDXRF)

The EDXRF measurements were performed at the Institute of Physics of the University of São Paulo (IF-USP), using the MINI X Model X-123 silicon-drift detector (SDD) Amptek portable EDXRF spectrometer equipped with one 2.5 W Ag X-ray tube and high-performance SDD (Si Drift 25 mm^2 × 500 μm/0.5 mil) Be (window/1.5″).

Laser-Induced Breakdown Spectroscopy

Laser-induced breakdown spectroscopy measurements were performed using a system consisted of a Q-switched neodymium-doped yttrium aluminum garnet (Nd:YAG) laser (Brilliant, Quantel, France) working at a fundamental wavelength of 1064 nm, pulses of 5 ns, with maximum energy of 230 ± 3 mJ, in a 6 mm diameter beam at a 10 Hz laser repetition rate. It used an ESA 3000 spectrometer (LLA Instruments, Germany) equipped with Echelle Optics and an intensified charge-coupled device, with signal acquisition from 200 nm to 780 nm in the emission spectra with resolution ($\lambda/\Delta\lambda$) between 10 000 and 20 000. The experimental setup used was assembled at Laboratório de Química Analítica do Centro de Energia Nuclear em Agricultura (CENA-USP). The plasma emission was collected by an optical system based on convergent plane-convex lens of fused silica with 50 and 80 mm focal lengths (LLA Instruments, GmbH, Germany). This optical system was coupled at slit entrance of spectrometer through of an optic fiber (1.5 m, 600 μm core). The lens to sample distance was set in 17.5 cm. Each ablation spectrum consisted of five laser shots of 50 $J{\cdot}cm^{-2}$, focalized at the same position of the sample, with delay time 2 μs and integration time 5 μs. For LIBS analysis, the tungsten emission line selected was 239.708 nm and the laser energy used was 365 mJ. Figure 1 depicts the scheme chosen in order to perform the point-by-point LIBS analysis for the PDMSUr (35% PWA) sample. Accordingly, with the LIBS analysis sequence shown in this figure, the integration of the peaks (see Figures S7a1, S7a2, S7b1, and S7b2, Supplemental Material) using Origin 6.0 software was performed in order to obtain the corresponding areas, aiming to the knowledge of the distribution pattern of tungsten concentrations (shown in Fig. 6). The integration limits (in wavelength units) of the tungsten (W) peaks were 239.553 nm and 239.837 nm. The distance between the consecutive points of analysis belonging to the same row was 1 mm and between the consecutive points of analysis belonging to the same column was 2 mm.[34–36,46]

Instrumental Neutron Activation Analysis

The PDMSUr-PWA films were irradiated in the IEA-R1 nuclear reactor at IPEN-CNEN/SP (IEA-R1, 3–4.5 MW, pool type) with a thermal neutron flux of 1.76 × 10^{12} neutrons cm^{-2} s^{-1}, time range per channel of 300–900 s, in order to determinate tungsten. IEA-R1 nuclear reactor has uranium enriched to 20% in the isotope ^{235}U as fuel and

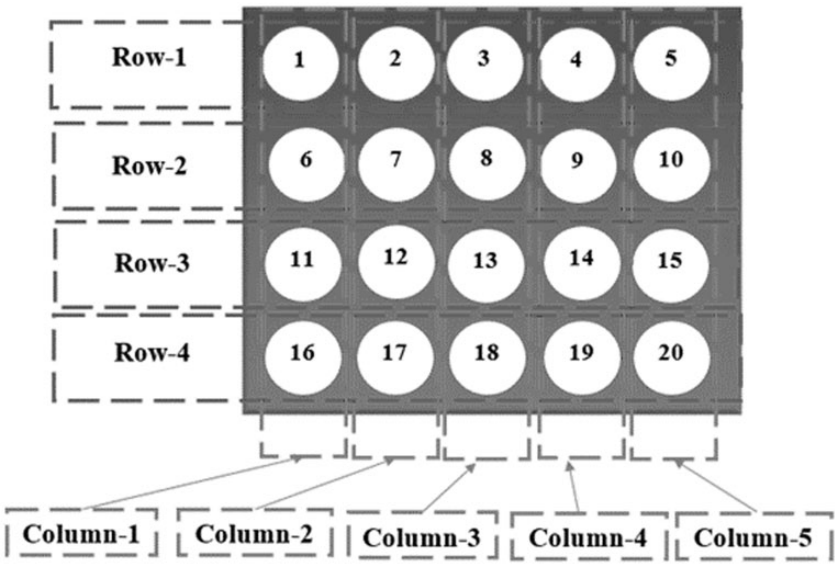

Figure 1. LIBS scanning sequence performed for the PDMSUr (35% PWA) sample.[42]

light water as moderator, operating at power of 4.5 MW. The nuclear reaction of neutron activation for tungsten nucleus is $^{186}W(n, \gamma)\ ^{187}W$. For the W^{187} isotope ($T_{1/2} = 24$ h; with energy $E\gamma = 479$, 481,552,618,687,745, 772 keV), an irradiation time of 30 s followed by a decay time of 2 h were used. The gamma spectrometer system used consisted of a high-purity germanium (HPGe) semiconductor detector with high resolution at full width half-maximum (FWHM), FWHM = 1.87 keV at 1332 keV of ^{60}Co, which was coupled to an ADCAM-ORTEC 919 E MCA analyzer and a micro-PC in order to measure the induced gamma ray activities. The source to sample distance was 12.5 cm.[42] The gamma spectral analyses evaluations were performed using the IDF computer code.[47] The NAA spectra are shown in the Supplemental Material.

Reference Materials

(i) SR-μXRF: The reference materials used for measurements were XRF calibration standards (99.9% pure or better) of zinc telluride (ZnTe) with areal density = 46.1 μg/cm^2(±5%) and gold (Au) with density = 47.2 μg/cm^2(±5%), provided by the Micromatter Company under the form of thin films on Mylar substrate (http://www.micromatter.com/XRFCalibration Standards.aspx).

(ii) NAA: The certified reference material used for the measurements was a foil of tungsten of high purity (99.95%) with 6 μm of thickness.

FEG-SEM: field emission gun scanning electron microscopy; attenuated total reflection Fourier transform mid-infrared (ATR FT-MIR): attenuated total reflectance Fourier transform mid-infrared; SR-μXRF: synchrotron radiation micro-X-ray fluorescence; SR-GIXRF: synchrotron radiation grazing incidence X-ray fluorescence; LIBS: laser-induced breakdown spectroscopy; NAA: neutron activation analysis.

Results and Discussion

Chemical Characterizations of the PDMSUr-PWA Films

Attenuated Total Reflectance Middle Infrared Spectroscopy. Figure 2 shows the spectra of pure PWA and the hybrid PU containing 35 wt% of phosphotungstic acid. Characteristic bands of Keggin structure of PWA, such as $W=O_d$ (984 cm^{-1}) and asymmetric stretching $W–O_b–W$ (889 cm^{-1}), are preserved inside the PDMSUr matrix; however, they presented a small shift. Such shifting is probably due to the interactions of PWA with the silicate regions, mainly silanol groups, as reported.[13,48] The same

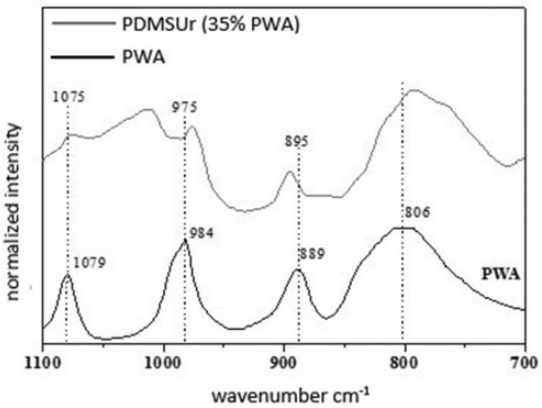

Figure 2. Infrared spectra of PDMSUr (35% PWA) and pristine PWA (light gray dotted line and dark gray solid line, respectively) in the region 1100–700 cm^{-1}.

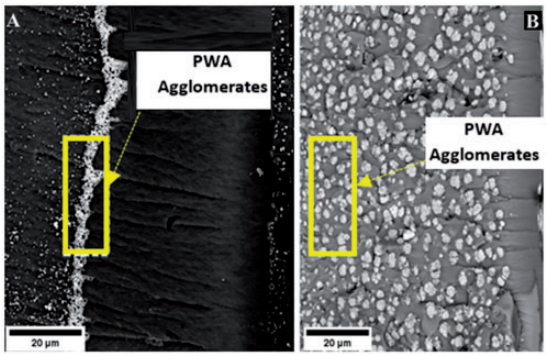

Figure 3. Cryo cross-section electron micrographs of PDMSUr containing: (a) 45 wt% PWA and (b) 55 wt% PWA. The agglomerates can be visualized by the yellow rectangles.

infrared profile was observed for the other prepared compositions.

The details of the groups conforming PDMSUr-PWA are illustrated in the corresponding infrared spectra (Figure S1, Supplemental Material).

Field Emission Gun Scanning Electron Microscopy

Images from cryogenic fracture obtained from FEG-SEM are shown in Fig. 3. Agglomerates of phosphotungstic acid (PWA) inside of PDMSUr matrix were observed in samples with high content of PWA, evidencing a phase segregation made of PWA clusters in composition 45 wt%/wt% and a homogenous cluster distribution in composition 55 wt%/wt%.[4]

The domains identified as PWA agglomerates were confirmed by wide angle X-ray scattering (WAXS) and XRD measurements. According to the EDX results published by Rossi de Aguiar et al., the shiny domains are mostly

composed of oxygen, tungsten, and phosphorous (Figure S2, Supplemental Material).[13]

Synchrotron Radiation X-ray Fluorescence

Synchrotron Radiation Micro-X-ray Fluorescence

Qualitative Determination by SR-μXRF: Maps of Tungsten Intensities. Figure 4 presents the SR-μXRF maps of the spatial distribution of tungsten (XRF line W–L_α) as function of the PWA content in the PDMSUr-PWA films. Up to 15.3% PWA content, tungsten mapping shows narrower range of W–L_α counting, except for the sample containing 8.3% PWA. The film containing 35% PWA shows the greatest homogeneity degree of W at surface* (between 42 000 and 54 000 counts predominantly, light gray color). For the other samples, the difference between maximum and minimum values of counts ranged between 40 000 and 54 000, besides exhibiting more color contrast, and thus showing less homogeneity of the tungsten (from PWA agglomerates) distribution on surface, insofar as the PWA concentration in the formulation increases. Thus, the SR-μXRF maps of tungsten agree with the FEG-SEM images, which shows phase separation for PWA contents >40 wt%/wt in the formulation.

At the 40–55% PWA range of content, the samples containing 47.6% PWA (Fig. 4g) and 50% PWA (Fig. 4h) show the highest (66 000) and lowest (45 000) top counts, respectively. This significant reduction of the tungsten intensities could indicate segregation in thickness.[42]

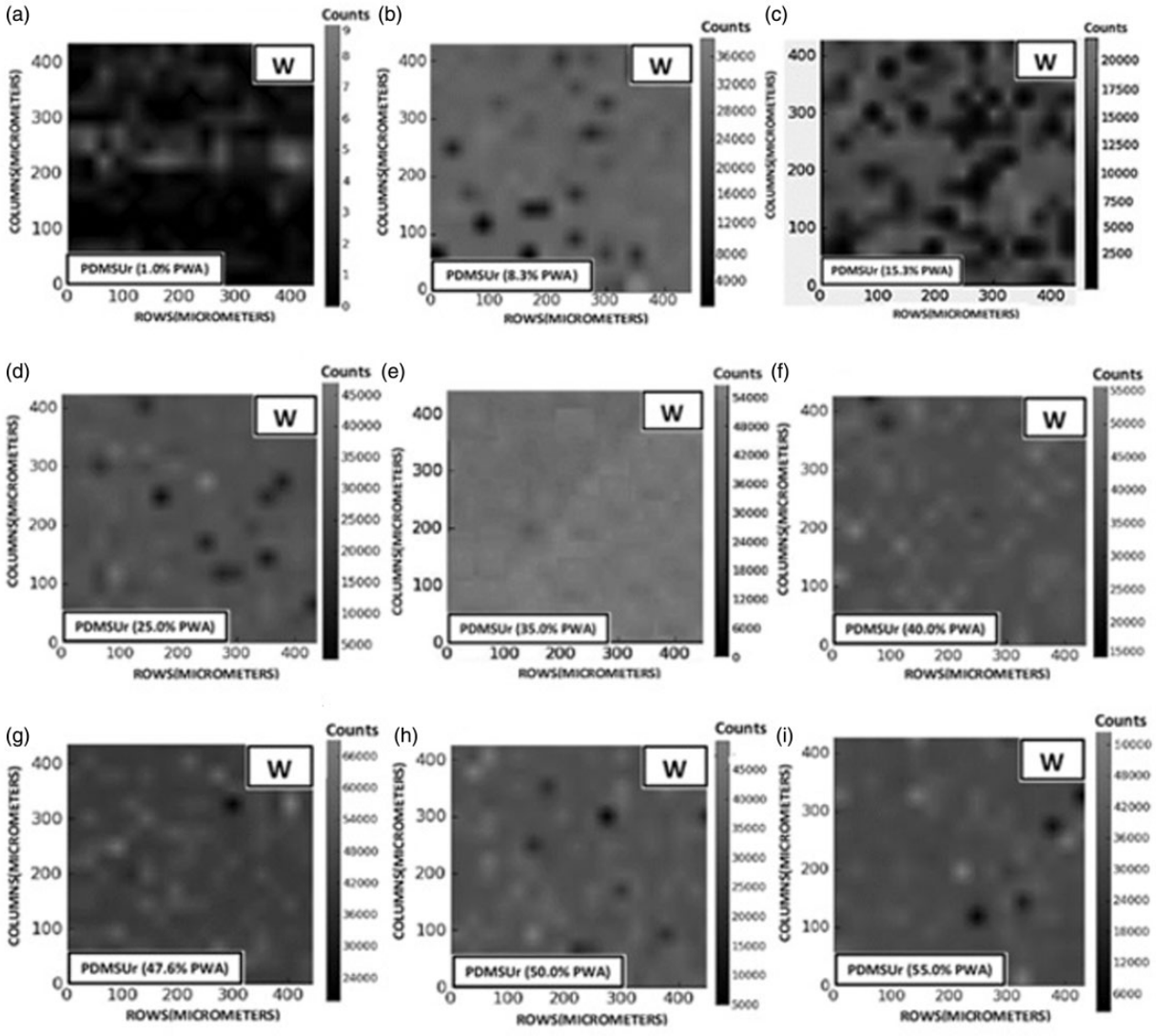

Figure 4. Two-dimensional SR-μXRF tungsten maps of intensities for PDMSUr-PWA films with different PWA contents. (a) 1.0 wt% PWA. (b) 8.3 wt% PWA. (c) 15.3 wt% PWA. (d) 25 wt% PWA. (e) 35 wt% PWA. (f) 40.0 wt% PWA. (g) 47.6 wt% PWA. (h) 50.0 wt% PWA. (i) 55.0 wt% PWA.

A similar conclusion can be achieved for W–L_α thickness mapping (Figure S3, Supplemental Material).

SR-μXRF Maps of the Spatial Correlation Between Silicon and Tungsten

Figure 5 shows the SR-μXRF maps of the spatial correlation between silicon (XRF line Si–K_α) and tungsten (XRF line W–L_α) intensities for the PDMSUr-PWA films.

Detailing the SR-μXRF Correlation Maps of the PDMSUr-PWA Films

From 1% PWA (Fig. 5a) to 8.3% PWA (Fig. 5b) it is revealed few common regions (spatial superposition) between the silicon + tungsten (white color). From this observation, a reduced interaction at surface between the silicon (from PDMS†) and tungsten (from PWA agglomerates) can be inferred, which is probably based on the different polarities

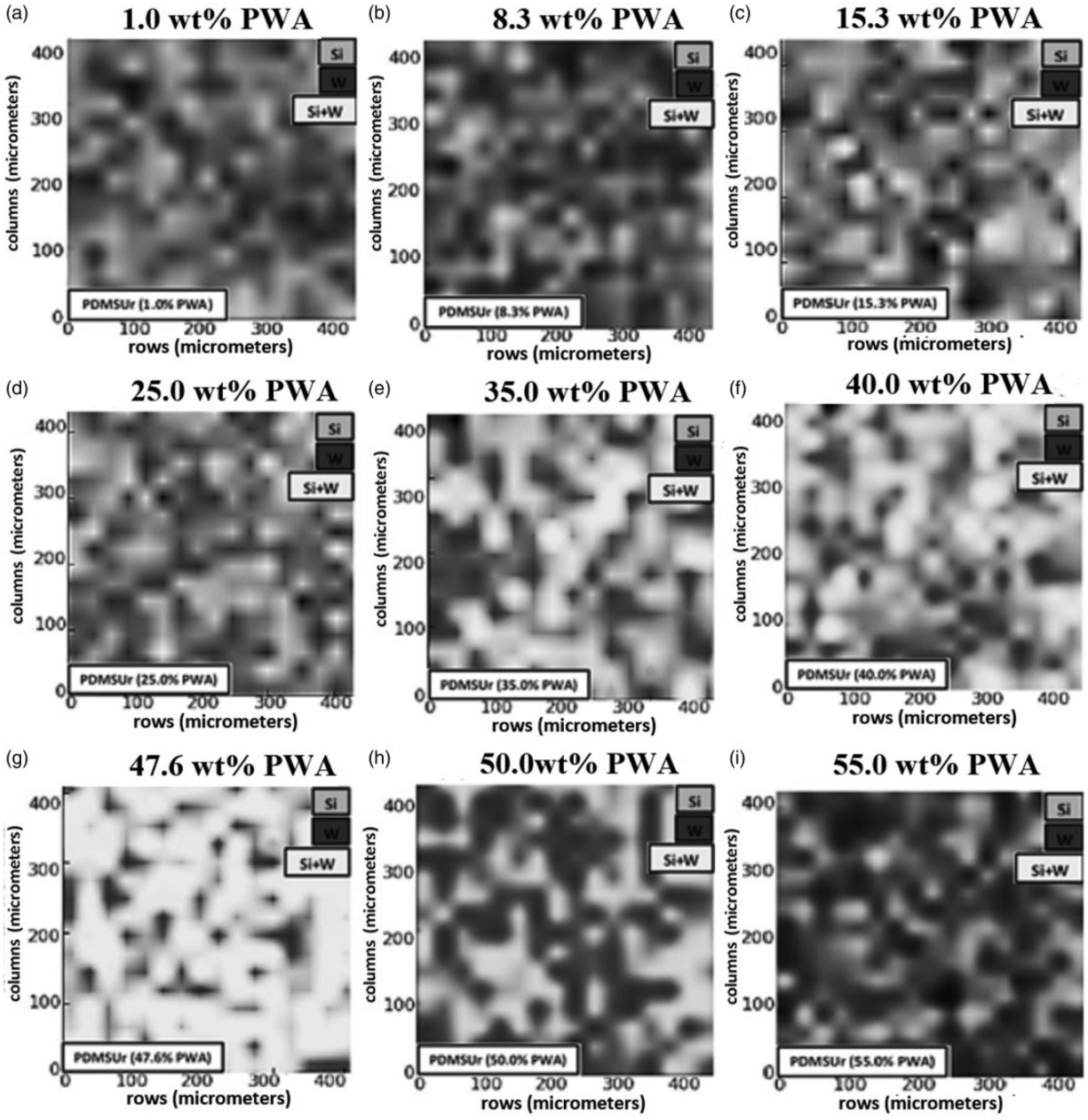

Figure 5. Two-dimensional SR-μXRF maps of correlation of intensities between silicon (light gray regions), tungsten (dark gray regions), and silicon + tungsten (white regions) of the PDMSUr-PWA samples as function of PWA content. (a) 1.0 wt% PWA. (b) 8.3 wt% PWA. (c) 15.3 wt% PWA. (d) 25 wt% PWA. (e) 35 wt% PWA. (f) 40.0 wt% PWA. (g) 47.6 wt% PWA. (h) 50.0 wt% PWA. (i) 55.0 wt% PWA.

of their respective molecular groups (PDMS: non-polar; PWA: polar) and on the different free surface energies of PDMS and PUs (for PDMS: 19–21 $mJ{\cdot}m^{-2}$, PU: ~40 $mJ{\cdot}m^{-2}$).[49,50]

From 1% PWA to 47.6% PWA (Figs. 5a to 5g, respectively), there is a progressive increase of the common regions of silicon + tungsten and the reduction of isolated silicon regions (light gray color). This observation shows the possible interaction between silicon and tungsten (from PWA agglomerates) in these films,[42] which is supported by the indicatives of ATR FT-MIR spectra about the formation of an ionic pair between the terminal groups W–O and $\equiv SiOH^{2+}$. Also, can be generated species ($\equiv Si{-}OH^{2+}$) ($H_2PW_{12}O_{40}^{-}$), as reported in Rossi de Aguiar et al.[13] Although spectra provide molecular information and SR-μXRF maps are in micrometric scale, PWA form agglomerates that can achieve this same scale, as illustrated in Fig. 3.

For values greater than or equal 50% PWA, the PDMSUr-PWA films show the diminution of common regions of silicon + tungsten and the increase of isolated tungsten and silicon regions (Figs. 5h and 5i).

This observation supports the hypothesis of significant inward diffusion of tungsten and silicon (although not necessarily at the same extension) from 50% PWA concentration level in these materials. This diffusion agrees with the chemical nature of the shiny domains observed in cross-section electron microscopy image for the PDMSUr (55% PWA) sample (Fig. 3). The composition of these shiny domains, in which the tungsten mass percentage is predominant, was described in the research realized by Rossi de Aguiar et al.[13]

From the spatial superposition degree between the silicon (XRF line Si–K_α) and tungsten (XRF line W–L_α) intensities, we can have hints about the possible interaction between these elements. Nonetheless, the alpha XRF lines of silicon only involve the inner electrons unlike the beta XRF lines of silicon (Si–K_β) that involve the external electrons. Thus, there is a possibility to have a notion about the chemical interactions of the silicon by means of the mapping of beta XRF lines of silicon (Si–K_β). For elements with atomic number (Z) less than 18 (e.g., $Z_{Silicon} = 14$), it is possible to obtain information about the interactions of their outer electrons from XRF analysis.[51–56] The corresponding SR-μXRF maps of the spatial correlation of intensities between Si–K_β/W–L_α XRF lines and Si–K_β/W–M_α lines are shown in Figures S4 and S5, respectively. From those maps, we can observe a high degree of the spatial superposition between Si–K_β and W–L_α lines and a moderate degree between Si–K_β and W–M_α lines, aiming to the chemical interactions between the silicon and tungsten. The interaction silicon–tungsten shown in Fig. 5 is supported by ATR FT-MIR analysis that reveals (Fig. 2) interactions between the silicates and PWA regions.[4]

Laser-Induced Breakdown Spectrometry

Semiquantitative Determination Using Laser-Induced Breakdown Spectroscopy

To the best knowledge of our research group, LIBS was used for the analysis of PDMSUr-PWA films to obtain the elemental distribution of tungsten. LIBS is used for the materials' characterization and chemical analysis of solids.[57] LIBS presents spatial resolution up to 20 μm and in-depth analysis at scale of microns or sub-microns (up to 50 nm). Thus, LIBS compared to XPS is a bulk method and compared to NAA is a surface method of analysis. The advantage to use LIBS is the possibility to obtain quick mapping (at a range from μs to fs)[57] of larger microscopic areas than obtained by SEM, EDX, or XPS elemental mapping. LIBS mapping can also provide semiquantitative data. LIBS spectra (Figures S8a and S8b, Supplemental Material) present differences of tungsten intensities, be by rows, columns, and/or diagonals, according to the sequence of points analyzed (Fig. 1).[42,57,58] Therefore, it is not possible to establish a homogeneous pattern of tungsten distribution. Figure 6 depicts the areas of the tungsten peaks corresponding to the LIBS spectra.

Figure 6 reveals the inhomogeneity of tungsten concentrations distribution at the millimetric level for the PDMSUr (35% PWA) sample. This result is complementary to the tungsten distribution pattern at micrometric level (Figure S7b, Supplemental Material). Thus, these differences of concentrations obtained from LIBS reflect chemical surface heterogeneity for these hybrid materials.[42]

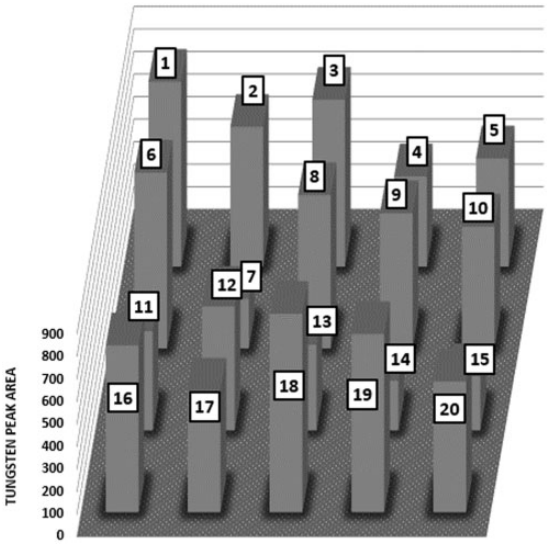

Figure 6. Three-dimensional representation of the areas of tungsten peaks analyzed by LIBS (rows: 1 to 4; columns: 1 to 5) for the PDMSUr (35% PWA) sample, according to the sequence of points analyzed (Fig. 1).

Instrumental Neutron Activation Analysis

Instrumental neutron activation analysis involves whole bulk analysis unlike SR-μXRF that can achieve a depth of hundredths of μm. Tungsten intensities (W^{187} isotope, with energy $E\gamma = 618$ keV) obtained by NAA analysis and their corresponding spectra are shown in the Supplemental Material (Figures S8a, S8b).

Analysis of Tungsten Segregation at the PDMSUr-PWA Films

Figure 7 depicts the ratios of concentrations of tungsten (obtained from SR-μXRF and NAA‡ analyses) and silicon§ (obtained from EDXRF) as a function of % PWA for the PDMSUr-PWA samples (see Acknowledgments and Table S1, Supplemental Material). The comparison of these methods of analysis enables us to know the existence of segregation of tungsten (as PWA) at thickness of the PDMSUr-PWA films.[42]

From the comparison of tungsten concentrations obtained using SR-μXRF and NAA for the PDMSUr-PWA films, it can be inferred that the distribution of tungsten concentrations presents segregation in the depth of the material.

Figure 7 reveals that from values higher than 40% PWA, the tungsten concentration determined by SR-μXRF is inferior to that obtained by NAA, evidencing the tungsten segregation across the thickness of the films. From values lower than 35% PWA, the tungsten concentration determined by SR-μXRF is superior to that obtained by NAA, evidencing tungsten segregation on surface of the films.[42] This segregation was also evidenced by SR-GIXRF analysis (Figure S6). The profiles of tungsten and silicon converge from approximately 35–40% PWA. To analyze these results, this graph is divided into three different regions, based on two hypotheses, as function of PWA content in the PDMSUr-PWA films:

(i) Region I, corresponding to the lowest PWA concentrations, could be based on the electrostatic interactions among PWA and amines groups, as was mentioned from the XPS analysis of Tungsten by Rossi Flores de Aguiar.[4] This region, in which the profiles of silicon and tungsten do not converge, would have predominance until ∼15% PWA.

(ii) Region II would constitute a transition zone between the Regions I and III. This region would have predominance from 15% PWA to 35% PWA approximately. The possible existent interactions would be among PWA with amine groups and APTES (source of Si).

(iii) Region III, corresponding to the medium-high PWA concentrations, could be based on the strong interaction between PWA and ormosil as reported in the literature.[59–61] There are also indications of this interaction (—Si ≡ ≡≡W—) at the corresponding SR-μXRF correlation maps of tungsten and silicon (Fig. 5; Figures S4 and S5). The Region III would have predominance since 35% PWA approximately. At values greater than 50% PWA, the concentrations of tungsten and silicon (more probably from APTES) undergo quasi-similar decrease, probably due to their diffusion across the thickness.[42] This hypothetic region supports the results of Rossi de Aguiar et al.[13] which mentioned that as the PWA content in the formulation of PDMSUr-PWA samples increases from 35 to 55%, a dramatic change in bulk morphology was observed.

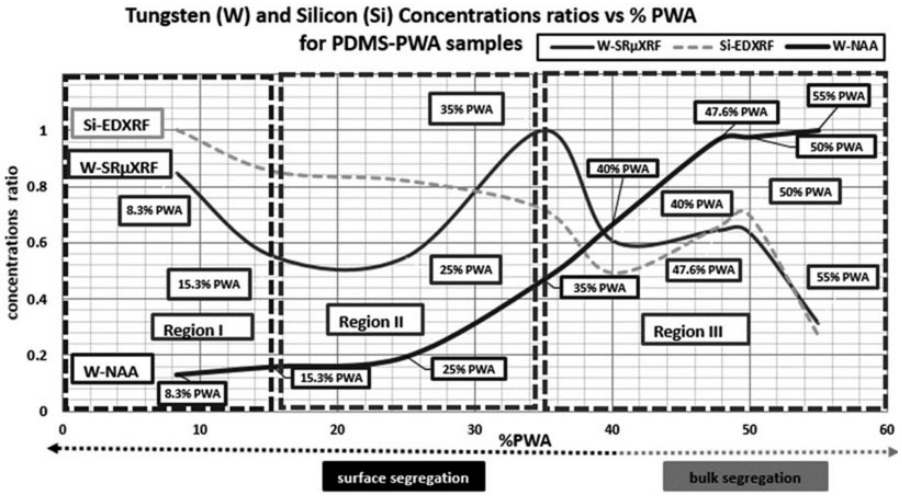

Figure 7. Tungsten concentration ratios obtained by SR-μXRF (dark gray bold line) and by NAA (black line) as reference value, and silicon concentration ratios obtained using EDXRF (light gray dashed line) as function of percentage PWA.

Correlation Between Structure and Properties of PDMSUr-PWA Films

The ATR FT-MIR analysis revealed that the molecular structure of phosphotungstates ($[PW_{12}O_{40}]^{3-}$) is kept quasi-unaltered inside of PDMSUr-PWA samples. Thus, from the distribution pattern of atomic tungsten, obtained by SR-μXRF, the distribution pattern of PWA (molecular tungsten) within these materials can also be inferred, because XRF is a nondestructive analysis. ATR FT-MIR spectra (Fig. 2) and the SR-μXRF maps of correlation between silicon and tungsten (Fig. 5; Figures S4 and S5, Supplemental Material) provide evidences about the possible interaction between these elements.[4,42] Previous studies showed that there is a strong interaction between the polyoxometalate and the ormosil regions, which are acting as hosts for the PWA molecules.[59,60] Protonated silanol ($\equiv Si–OH_2^+$) can act as counter-ion for the polyanion $[PW_{12}O_{40}]^{3-}$, generating species $(\equiv Si–OH_2^+)(H_2PW_{12}O_{40}^-)$.[61] Also, materials containing amine groups, such as the analyzed hybrid PDMSUr, can be functionalized with PWA using electrostatic interactions.[62,63] An unpublished work of our group has revealed, from XPS results, the existence of protonated amine groups within the information depth of 10 nm approximately at the PDMSUr-PWA films. This finding indicates that the heteropolyacid (PWA) can electrostatically interact with free amines or unreacted amines, affording the formation of such protonated species. The characteristic tungsten doublets $W4f_{5/2}$ and $W4f_{7/2}$ were also identified in these films, which is further evidence of the presence of this element.[4]

Rossi de Aguiar et al.[13] published that during the nanoindentation measurements, PDMSUr-PWA films exhibited high values of hardness (20–60 MPa). This hardness increases directly with the mass percentage of PWA, being the PDMSUr (55% PWA) sample that has shown the stiffest surface. The increase of stiffness is based on the fact that the presence of PWA stimulates the kinetics of hydrolysis and the polycondensation of alkoxysilane groups inside the PDMSUr matrix. These chemical reactions increase the molar fraction value of ceramic mass, thus increasing the scratch resistance and deformation on the surface of this hybrid material, consequently, enhancing its hardness. Furthermore, PWA can also improve the action of ormosil on the reinforcement of the hybrid material by means of an increase in cross-linking density.[4,13]

From the FEG-SEM image (Fig. 3), NAA tungsten intensities (Figure S8, Supplemental Material) and the ratio of the tungsten concentrations (Fig. 7) for the PDMSUr (55% PWA) sample confirm the significant segregation of tungsten across the thickness at concentration levels higher than 50% PWA for PDMSUr-PWA films.[42] Also, it can be observed that this segregation starts to manifest at the 35%–50% PWA range.

For the PDMSUr (1% PWA) sample, the corresponding SR-μXRF map (Fig. 4a) and from previous XPS results of Rossi Flores de Aguiar[4] reveal that in the lowest PWA concentrations, the tungsten is present on the top of the surface (few nanometers of depth) at the PDMSUr-PWA films.[4,42] In the SR-μXRF map (Fig. 5b), the concentration ratio for tungsten (Fig. 7), the SR-GIXRF test (Figure S6, Supplemental Material), and the evidence of the segregation of tungsten on the surface of these films have predominance until approximately 15.3% PWA.

From the LIBS analysis (Fig. 6; Figures S7a and S7b, Supplemental Material) corresponding to the PDMSUr (35% PWA) sample, the heterogeneity at millimetric level for tungsten distribution pattern at PDMSUr-PWA films can be inferred.[42]

Besides the PWA segregation in thickness of these hybrid materials, the PWA is also finely dispersed at films with PWA content <35 wt/wt%. At PWA concentrations >35 wt/wt%, there is a significant change observed at thickness, as reported by Rossi de Aguiar et al.[13] PWA kept its structure inside of these hybrid films through interactions between the organic matrix of PDMSUr and silanol from the inorganic part (ormosil), as shown by ATR FT-MIR spectra. PDMS is incompatible with PU due to their different nature (PDMS: non-polar and PU: polar), due to their different solubility parameters, and the weak interaction between them. This incompatibility generates phase segregation in the morphology of the PDMS/PU system. In addition to the nature of the interface, the dimensions of the organic and inorganic phases can cause variations in the properties of the hybrids, such as changes in thermal behavior, rheology, stability of solutions, and in the morphology of the material.

PDMSUr-PWA films contain two different classes of materials in their composition, which supplied flexibility (PDMS) and rigidity (ormosil/PWA), joined through covalent bonds or intermolecular interactions. The agglomerates identified by electron microscopy as PWA in Fig. 3 were also identified by WAXS, which results have presented ordered domains.[13] From DRX results, the formation of polyhedral oligomeric silsesquioxanes (POSS) and the formation of ordered domains inside the hybrid organosilicate network, induced by PWA, were suggested. Thus, PDMSUr-PWA films constitute semicrystalline materials.[13]

In the proposed structure of this hybrid material, organic (corresponding to PDMS) and inorganic domains of ormosil are covalently connected through urethane bonds. Ormosil regions constitute a host structure for PWA, which acts as catalyst in the hydrolysis and polycondensation reactions, providing properties such as proton conductivity and increased elastic modulus and hardness. The hardening of the surface and elastic modulus of PDMSUr-PWA films is generally proportional to the density of the crosslinking, which is in turn directly related to PWA content. Sol–gel

reactions lead to the production of ormosil or silica regions providing rigidity to the material.[4,13]

Based on all these results, models of tungsten distribution in function of %PWA were developed, which are shown in Fig. 8 (previous steps for elaborating the models are shown in Figure S9, Supplemental Material).

Detailing Some Aspects of Concentration Gradients in the Design of Model Proposed

Vertical Gradient

From a comparison of SR-μXRF and NAA results for the PDMSUr-PWA films, it can be inferred that the distribution of tungsten concentration presents segregation in the depth of the material. During the process of formation of these films, insofar that the PWA content increases in turn also the speed of formation of the silicates three-dimensional network (as indicated by the ^{29}Si NMR characterization), by means of hydrolysis and condensation reactions, favoring the increase in the stiffness of these materials, consequently the elastic modulus and hardness.[13] According to the model proposed by Rossi de Aguiar et al., the organic and inorganic domains are covalently connected.[13] FT-MIR spectra indicate interactions among PWA and silicate regions ($\equiv Si–OH^{2+}$).($H_2PW_{12}O_{40}^-$) and also with the organic matrix (possibly through Coulombic interactions).

Lateral Gradient

XPS[4] and SR-GIXRF[42] results showed the presence of tungsten at tenths and tens of nanometers of depth, respectively. However, due to that the PDMS has a lower surface energy in this hybrid material; in addition to non-polarity of PDMS and the polarity of PWA, the presence of tungsten is

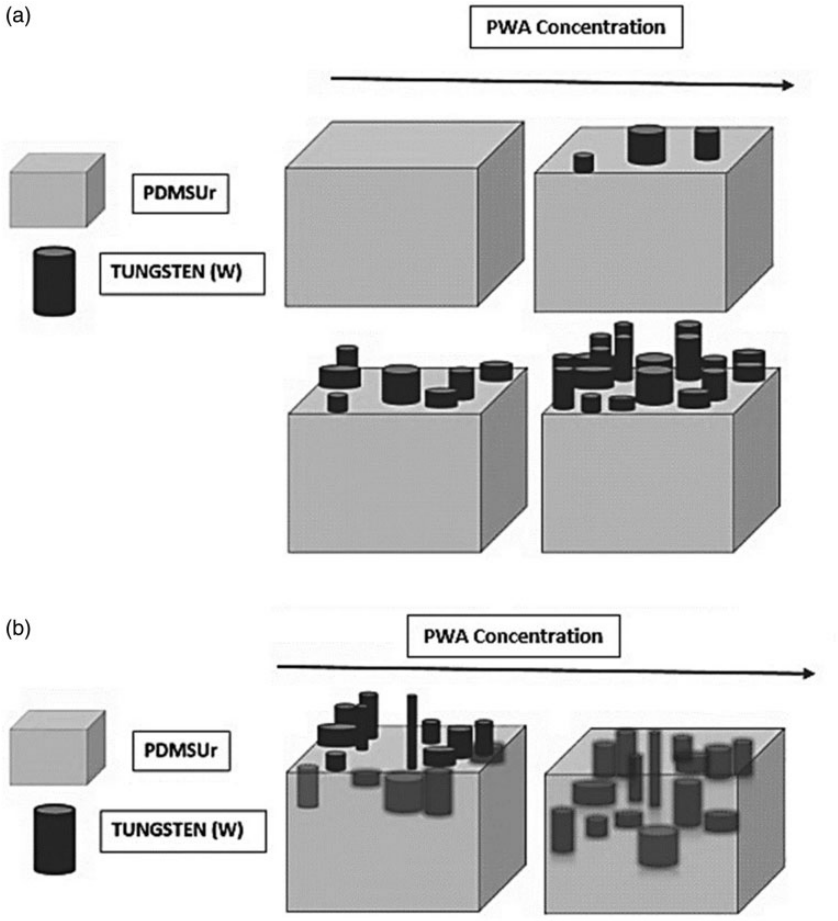

Figure 8. Models of tungsten distribution for PDMSUr-PWA films. (a) PDMSUr-PWA films, in which tungsten (as PWA) segregation in surface is predominant, for PWA concentrations lower than 50% wt/wt. (b) PDMSUr-PWA films, in which tungsten (as PWA) segregation across the thickness is predominant, for PWA concentrations higher than 50% wt/wt.

Table II. Tungsten concentrations obtained using SR-μXRF42 and NAA42 for the PDMSUr-PWA films.

PDMSUr-PWA	[PWA] (wt/wt%)[a]	[W] (wt/wt%) SR-μXRF	[W] (wt/wt%) NAA
PDMSUr (8.3% PWA)	8.3	9.3 ± 2.3	8.6 ± 3.3
PDMSUr (15.3% PWA)	15.3	23.0 ± 6.6	18.2 ± 0.9
PDMSUr (25% PWA)	25	33.2 ± 9.6	35.3 ± 1.8
PDMSUr (35% PWA)	35	37.7 ± 7.4	39.6 ± 2.0
PDMSUr (40% PWA)	40	38.4 ± 10.9	41.9 ± 2.0
PDMSUr (47.6% PWA)	47.6	40.4 ± 11.5	38.7 ± 2.0
PDMSUr (50% PWA)	50	40.7 ± 13.0	47.2 ± 2.5
PDMSUr (55% PWA)	55	9.3 ± 2.3	44.7 ± 2.3

[a]Relative to the total mass of PDMSUr precursors (CCPDMS + APTES) without solvent.[4,13]

less at tenths than at tens of nm. LIBS results (Figure 6) and SR-μXRF maps (Figs. 4 and 5) reflect chemical surface heterogeneity of tungsten for these hybrid materials at micrometric level.

Conclusion

Hybrid poly(dimethylsiloxane)-derived hydroxyurethanes films containing phosphotungstates (PDMSUr-PWA) were characterized and analyzed by ATR FT-MIR, FEG-SEM, SR-μXRF, SR-GIXRF, LIBS, and NAA. From these results, it can be concluded that there is a predominant tungsten (from phosphotungstates $[PW_{12}O_{40}]^{3-}$) segregation across the thickness of the films at PWA concentrations higher than 50 wt%/wt. However, this segregation starts to manifest at the concentration range [35%–50% PWA]. From previous studies, at this range a dramatic change of the bulk morphology of these materials was observed. At PWA concentrations less than 35% wt/wt, the tungsten segregation at surface of these films is predominant, based probably on the electrostatic interactions among PWA with ormosil and amine groups. There are conditions for a significant interaction between the silicon and tungsten in these materials since 15% PWA approximately, as it was revealed by the SR-μXRF correlation maps, supporting the strong interaction between ormosil and phosphotungstates reported in literature. At PWA concentrations less than 15 wt%/wt, the electrostatic interactions between PWA and amine groups possibly predominate. At the top surface (tenths of nanometers of depth), there is no significant interaction between tungsten (from PWA) and silicon (from PDMS), probably due to the different polarities of their respective molecular groups. However, at micrometers of depth, the tungsten can interact with the silicon (from APTES), as could be observed at ATR FT-MIR spectra. More in-depth studies are necessary for the understanding of these interactions. From FEG-SEM/SR-μXRF results of this present study in combination with WAXS/XRD/EDX results from previous studies, the presence of molecular tungsten (as phosphotungstates) in the domains of PDMSUr-PWA films was proven. Inhomogeneities of the tungsten concentration distribution patterns at micrometric and millimetric levels was demonstrated using SR-μXRF and LIBS analyses, respectively. This inhomogeneity of tungsten may play an important role in the mechanical properties of these films (elastic modulus and hardness). From the correlation of structure and properties of the PDMSUr-PWA films, models of tungsten/phosphotungstates distribution in function of PWA concentration were elaborated.

Acknowledgments

The authors thank Dr. Carlos Perez for his help at the XRF measurements done at Brazilian Synchrotron Light Source (LNLS). The authors also extend their gratitude to Prof. Dr. Francisco Krug and Dr. Lidiane C. Nunes of the Analytical Chemistry Laboratory of CENA-USP ("Henrique Bergamin Filho") for the LIBS measurements, and Prof. Dra. Márcia A. Rizzutto for the EDXRF measurements performed at the Institute of Physics of the University of São Paulo (IF-USP). Finally, Orlando Elguera Ysnaga thanks Dr. Michael Noeske from Fraunhofer Institut für Fertigungstechnik und Angewandte Materialforschung (IFAM), Bremen-Germany, and the Inorganic Hybrid Materials Chemistry Group (GQMATHI-IQSC-USP) of the Institute of Chemistry of São Carlos, University of São Paulo, Brazil, for the discussions and suggestions.

Declaration of Conflicting Interests

The author(s) declared no potential conflicts of interest with respect to the research, authorship, and/or publication of this article.

Funding

The author(s) disclosed receipt of the following financial support for the research, authorship, and/or publication of this article: The authors thank the São Paulo Research Foundation (FAPESP) (research grants 2011/08120-0, 2011/06019-0, and 2013/05279-3) and the CNPq Brazilian agency for the financial support (research grants 141880/2011-2 and 160515/2011-4); the CNPEM-LNLS facilities for SR-GIXRF and SR-μXRF measurements (proposal numbers: XAFS1 14254 and XAFS1 14257, respectively).

ORCID iD

Orlando Elguera Ysnaga https://orcid.org/0000-0002-6956-0204

Supplemental Material

The supplemental material mentioned in the text, consisting of figures and tables, is available in the online version of the journal.

Notes

* The information depth obtained by applying the method SR-μXRF is at the range of 10–1000 μm approximately.

† There is migration of the PDMS, due to its low surface energy, to the air–polymer interface at PDMS-based polyurethane copolymers.
‡ NAA is the reference method for tungsten determination.
§ Silicon concentration profile was determined from EDXRF measurements.

References

1. J. Vega, S. Madrigal, J. Martínez. "Thermoplastic Polyurethanes-Fumed Silica Composites: Influence of NCO/OH in the Study of Thermal and Rheological Properties and Morphological Characteristics". In: A. Zaki, E. Sonbati, editors. Thermoplastic–Composite Materials. Croatia: Intech, 2012. Pp. 11–25.
2. G. Oertel. Polyurethane Handbook. Munich: Hanser Publishers, 1985. Pp. 7–116.
3. W. Hui, W. Qingsong, H. Jia-Jia, et al. "Study on the Pyrolytic Behaviors and Kinetics of Rigid Polyurethane Foams". Procedia Eng. 2013. 52. 377–385.
4. K. Rossi Flores de Aguiar. Síntese de Hidroxiuretana-Poli(dimetilsiloxano) com Diferentes Terminações de Cadeia via Fixação de CO_2: Síntese, Caracterizações e Aplicações. [Doctor of Science in Analytical and Inorganic Chemistry, Thesis]. São Paulo-Brasil: Universidade de São Paulo (IQSC-USP), 2015.
5. T. Bürgel, M. Fedtke. "Epoxy Resins with Cyclic Carbonate Structures". Polym. Bull. 1993. 30: 61.
6. B. Sweileh, Y. Al-Hiari, M. Kailani, et al. "Synthesis and Characterization of Polycarbonates by Melt Phase Interchange Reactions of Alkylene and Arylene Diacetates with Alkylene and Arylene Diphenyl Dicarbonates". Molecules. 2010. 15(5): 3661–3682.
7. O. Figovsky, L. Shapolov, N. Blank. Cyclocarbonate Groups Containing Hydroxyamine Oligomers from Epoxycyclocarbonates. US Patent 6 407198 B1. 2002.
8. M. Aresta, A. Dibenedetto, A. Angelini. "Catalysis for the Valorization of Exhaust Carbon: from CO_2 to Chemicals, Materials, and Fuels. Technological Use of CO_2". Chem. Rev. 2014. 114: 1709–1742.
9. L. Wang, Q. Ji, T. Glass, et al. "Synthesis and Characterization of Organosiloxane Modified Segmented Polyether Polyurethanes". Polymer. 2000. 41: 5083–5093.
10. M. Pergal, J. Dzunuzovic, R. Poreba, et al. "Surface and Thermomechanical Characterization of Polyurethane Networks Based on Poly(Dimethylsiloxane) and Hyperbranched Polyester". Exp. Polym. Lett. 2013. 7(10): 806–820.
11. E. Sollier, C. Murray, P. Maoddia, et al. "Rapid Prototyping Polymers for Microfluidic Devices and High-Pressure Injections". Lab Chip. 2011. 11: 3752–3765.
12. K.R. Aguiar, V.G. Santos, M. Eberlin, et al. "Efficient Greensynthesis of Bis(Cyclic Carbonate) Poly(Dimethylsiloxane) Derivative Using CO_2 Addition: A Novel Precursor for Synthesis of Urethanes". RSC Adv. 2014. 4(46): 24334–24343.
13. K.M.F. Rossi de Aguiar, E.P. Ferreira-Neto, S. Blunk, et al. "Hybrid Urethanesil Coatings for Inorganic Surfaces Produced by Isocyanate-Free and Sol-Gel Routes: Synthesis and Characterization". RSC Adv. 2016. 6(23): 19160–19172.
14. R. Peña-Alonso, F. Rubio, J. Rubio. "The Role of Γ-Aminopropyltriethoxysilane (Γ-APS) on Thermal Stability of TEOS-PDMS Ormosils". J. Sol-Gel Sci. Technol. 2005. 36(1): 77–85.
15. J. Mosa, A. Durán, M. Aparicio. "Epoxy-Polystyrene-Silica Sol-Gel Membranes with High Proton Conductivity by Combination of Sulfonation and Tungstophosphoric Acid Doping". J. Membr. Sci. 2010. 361(1–2): 135–142.
16. R. Piva, M. Rocha, D. Piva, et al. "Acidic Dressing Based on Agarose/$Cs_{2.5}H_{0.5}PW_{12}O_{40}$ Nanocomposite for Infection Control in Wound Care". ACS Appl. Mater. Interfaces. 2018. 10(37): 30963–30972.
17. European Synchrotron Radiation Facility (ESFR). 2015. http://www.esrf.eu/about/synchrotron-science [accessed April 3, 2015].
18. P. Willmott. "Synchrotron Physics". In: Introduction to Synchrotron Radiation: Techniques and Applications. Chichester, UK: John Wiley and Sons, 2011. Chap. 3, Pp. 39–86.
19. K. Janssens, F. Adams, A. Rindbly. Microscopic X-ray Fluorescence Analysis. Chichester, UK: John Wiley and Sons, Ltd., 2000.
20. B. Patterson, G. Havrilla, J. Schoonover. "Elemental and Molecular Characterization of Aged Polydimethylsiloxane Foams". Appl. Spectrosc. 2006. 60(10): 1103–1110.
21. B. Patterson, G. Havrilla. "Confocal Micro X-ray Fluorescence a New Paradigm in 3D Elemental Imaging for Materials Characterization". Microsc. Microanal. 2008. 14(S2): 1088–1089.
22. F. Adams. "Synchrotron X-ray Fluorescence Analysis in Environmental and Earth Sciences". EPJ Web Conf. 2010. 9: 165–180.
23. A. Balerna, S. Mobilio. "Introduction to Synchrotron Radiation". In: S. Mobilio, F. Boscherini, C. Meneghini, editors. Synchrotron Radiation: Basics, Methods and Applications. Berlin, Germany: Springer-Berlin, 2015. Pp. 3–28.
24. K. Janssens, L. Vincze, A. Aerts, et al. "Synchrotron Radiation Induced X-ray Microfluorescence Analysis". Mikrochim. Acta Suppl. 1996. 13: 87–115.
25. K. Janssens, L. Vincze, F. Adams. "Synchrotron Radiation-Induced X-ray Microanalysis". Anal. Chim. Acta. 1993. 283: 98–119.
26. H. Sitepu, M. Kopylova, D. Quirt, et al. "Synchrotron Micro-X-ray Fluorescence Analysis of Natural Diamonds: First Steps in Identification of Mineral Inclusions In Situ". Am. Mineral. 2005. 90: 1740–1747.
27. E. Ferreira-Neto, S. Ullah, O. Elguera Ysnaga, et al. "Zn^{2+} Doped Ormosil–Phosphotungstate Hybrid Films with Enhanced Photochromic Response". J. Sol-Gel Sci. Technol. 2014. 72(2): 290–300.
28. F. Ferreira, T. Amaral, O. Elguera Ysnaga, et al. "Structure–Property Relationship of New Polymide–Organically Modified Silicate–Phosphotungstic Acid Hybrid Material System". J. Mater. Sci. 2016. 51: 4815–4824.
29. B. Kanngiesser, M. Haschke. "Methodological Developments and Applications. Micro X-ray Fluorescence Spectroscopy". In: B. Beckhoff, B. Kanngiesser, N. Langhoff, et al., editors. Handbook of Practical X-ray Fluorescence Analysis. Berlin, Heidelberg: Springer-Verlag, 2006, Chap. 7, Pp. 433–553.
30. A. Markowicz. "X-ray Physics". In: R. Van Grieken, A. Markowicz, editors. Handbook of X-ray Spectrometry. New York: Marcel Dekker, 2002. Pp. 1–38.
31. H. Ainginger, P. Wobrauschek. "A Method for Quantitative X-ray Fluorescence Analysis in Nanogram Region". Nucl. Instrum. Methods. 1974. 114(1): 157–158.
32. J. Kawai, K. Hayashi, H. Amano, et al. "Surface Analysis of Si/W Multilayer Using Total Reflection X-ray Photoelectron Spectroscopy". J. Electron Spectrosc. Relat. Phenom. 1998. 88–91: 787–791.
33. L. Gonçalves, E. Ferreira-Neto, S. Ullah, et al. "Enhanced Photochromic Response of Ormosil–Phosphotungstate Nanocomposite Coatings Doped with TiO_2 Nanoparticles". J. Sol-Gel Sci. Technol. 2015. 76(2): 386–394.
34. L. Sancey, V. Motto-Ros, S. Kotb, et al. "Laser-Induced Breakdown Spectroscopy: A New Approach for Nanoparticle's Mapping and Quantification in Organ Tissue". J. Visualized Exp. 2014. 88: 51353.
35. V. Pinon, M. Mateo, N. Gines. "Laser-Induced Breakdown Spectroscopy for Chemical Mapping of Materials". Appl. Spectrosc. Rev. 2013. 48(5): 357–383.
36. L. Peruchi, L. Nunes, G. Arantes de Carvalho, et al. "Determination of Inorganic Nutrients in Wheat Flour by Laser-Induced Breakdown Spectroscopy and Energy Dispersive X-ray Fluorescence Spectrometry". Spectrochim. Acta, Part B. 2014. 100: 129–136.
37. L. Hamidatou, H. Slamene, T. Akhal, et al. "Concepts, Instrumentation and Techniques of Neutron Activation Analysis". In: F. Kharfi, editor.

Imaging and Radioanalytical Techniques in Interdisciplinary Research: Fundamentals and Cutting-Edge Applications. London: IntechOpen, 2013. https://www.intechopen.com/books/imaging-and-radioanalytical-techniques-in-interdisciplinary-research-fundamentals-and-cutting-edge-applications/concepts-instrumentation-and-techniques-of-neutron-activation-analysis [accessed July 6 2020].

38. R. Nadkarni, B. Haldar. "Sub-Stoichiometric Determination of Tungsten by Neutron Activation Analysis". J. Radioanal. Chem. 1971. 8(1): 45–51.
39. N. Rajurkar, D. Zinjad. "Instrumental Neutron Activation Analysis of Tungsten in Various Steel Samples". J. Radioanal. Chem. 1988. 127(5): 333–340.
40. S. Srivastava, S. Bhaisare, D. Wagh, et al. "Analysis of Tungsten in Low Grade Ores and Geological Samples". Bull. Mater. Sci. 1996. 19(2): 331–343.
41. S. Morrison, C. Beck, J. Bowen, et al. "Determination of Tungsten in Geochemical Reference Material Basalt Columbia River 2 by Radiochemical Neutron Activation Analysis and Inductively Coupled Plasma Mass Spectrometry". J. Radioanal. Nucl. Chem. 2017. 311(1): 749–754.
42. O.A. Elguera Ysnaga. Métodos de Análise de Materiais Híbridos: Um Estudo Comparativo Entre Fluorescência de Raios-X Com Detecção Dispersiva em Energia Usando Fonte Tradicional e Luz Síncrotron. [Doctor of Science in Analytical and Inorganic Chemistry, Thesis]. São Carlos, São Paulo-Brasil: Universidade de São Paulo (IQSC-USP), 2015. Pp. 249–301.
43. C. Pérez, M. Radtke, H. Sánchez, et al. "Synchrotron Radiation X-ray Fluorescence at the LNLS: Beamline Instrumentation and Experiments". X-ray Spectrom. 1999. 28(5): 320–326.
44. V. Solé, E. Papillon, M. Cotte, et al. "A Multiplatform Code for the Analysis of Energy-Dispersive X-ray Fluorescence Spectra". Spectrochim. Acta, Part B. 1999. 62(1): 63–68.
45. PyMca Home. 2015. http://pymca.sourceforge.net/documentation.html [accessed April 3 2015].
46. L. Nunes. Estratégias Quimiométricas Para Análise de Plantas Por Espectrometria de Emissão Óptica Com Plasma Induzido por Laser. [Doctor of Science in Analytical Chemistry, Thesis]. São Carlos, São Paulo-Brasil: Universidade Federal de São Carlos, 2010.
47. P. Gouffon. Manual Do Programa IDEFIX. São Paulo, Brazil: Instituto de Física da Universidade de São Paulo (IFUSP), 1987.
48. U.L. Štangar, N. Grošelj, B. Orel, et al. "Structure of and Interactions Between P/Siwa Keggin Nanocrystals Dispersed in an Organically Modified Electrolyte Membrane". Chem. Mater. 2000. 12(12): 3745–3753.
49. S. Vudayagiri, M. Junker, A. Skov. "Factors Affecting the Surface and Release Properties of Thin Polydimethylsiloxane Films". Polymer J. 2013. 45: 871–878.
50. P. Król, B. Król. "Surface Free Energy of Polyurethane Coatings with Improved Hydrophobicity". Colloid Polym. Sci. 2012. 290(10): 879–893.
51. H.A. Liebhafsky, H.G. Pfeiffer, E.H. Winslow, et al. X-ray Absorption and Emission in Analytical Chemistry: Spectrochemical Analysis with X-rays. New York: John Wiley and Sons, 1960.
52. V.R. Hoffmann. G.J. Miller. Solids and Surfaces: A Chemist's View on Bonding in Extended Structures. New York: VCH Publishers, 1989.
53. G. Deodhar. "Some Investigations in Rontgen Spectra Part II. X-ray Spectra and Chemical Combination. Sulphur". Proc. R. Soc. A. 1931. 131(818): 647–658.
54. A. Meisel, G. Leonhardt, R. Szargan. "X-Ray Spectroscopic Studies of the Band Structure of Solids". In: R. Gomer, editor. X-ray Spectra and Chemical Binding. Springer Series in Chemical Physics. Berlin: Springer-Verlag, 1989. Vol.37, Chap. 2, Pp.36–55.
55. A. Compton, S. Allison. X-rays in Theory and Experiment. Chicago: D. Van Nostrand Company, Inc., 1967.
56. T. Wetterblad. "Die Kβ1-Linien von Natrium, Magnesium und Aluminium und die Abhängigkeit ihrer Wellenlängen von der Chemischen Bindung". Z. Phys. 1927. 42(8): 603–610.
57. S.S. Mao. "Laser Ablation: Fundamentals and Applications". Presented at: Lawrence Berkeley National Laboratory, University of California at Berkeley; July 20, 2004.
58. S.J. Rehse. "Laser-Induced Breakdown Spectroscopy (LIBS). Principles of and Recent Advances in Laser Micro/Nano Manufacturing Processes". Presented at: Principles of and Recent Advances in Laser Micro/Nano Manufacturing Processes. Evanston, Illinois; June 1–4, 2010.
59. A. Popa, V. Sasca, E. Kiss, et al. "Studies in Structural Characterization of Silica-Heteropolyacids Composites Prepared by Sol-Gel Method". Mat. Chem. Phys. 2010. 119(3): 465–470.
60. D. Pito, I. Matos, I. Fonseca, et al. "Methoxylation of α-Pinene Over Heteropolyacids Immobilized in Silica". Appl. Catal., A. 2010. 373: 140–146.
61. K.-V. Peinemann, S. Pereira Nunes. Membranes for Energy Conversion. Weinheim, Germany: Wiley-VCH Verlag GmbH, 2008.
62. W. Zhang, Q. Zhao, T. Liu, et al. "Phosphotungstic Acid Immobilized on Amine-Grafted Graphene Oxide as Acid/Base Bifunctional Catalyst for One-Pot Tandem Reaction". Ind. Eng. Chem. Res. 2014. 53(4): 1437–1441.
63. X. Wang, Y. Huang, Z. Lin, et al. "Phosphotungstic Acid Encapsulated in the Meso-Cages of Amine-Functionalized Metal-Organic Frameworks for Catalytic Oxidative Desulfurization". Dalton Trans. 2014. 43(31): 11950–11958.